Supplementary Materials: Prediction of Weyl semimetal and AFM topological insulator phases in Bi_2MnSe_4

Sugata Chowdhury[1*], Kevin F. Garrity[1], Francesca Tavazza[1]

[1]Materials Measurement Laboratory, National Institute for Standards and Technology, Gaithersburg, MD 20899

## Supplementary materials: Contains the following sections:

Section SI – Structures and Bi_3Se_4 band structure.

Table S1: The lattice parameters of different crystal structures.

Crystal Structure	a (Å)			c (Å)		
	Exp	Non-Rel	Rel	Exp	Non-Rel	Rel
B_3Se_4	4.23	4.31	4.28	40.5	41.11	40.9
Bi_2PbSe_4	-	4.37	4.31	-	41.85	41.67
Bi_2PbTe_4	4.44	4.55	4.49	41.61	42.41	42.05
Bi_2MnSe_4	4.197	4.29	4.22	37.797	38.94	38.52
Bi_2MnTe_4	4.334	4.45	4.37	40.91	41.82	41.38

Fig. S1: Scalar-relativistic (a) and full-relativistic bandstructure of Bi_3Se_4 using PBE functional along the high symmetry in k-space of a Brillouin zone with space group $R\bar{3}m$. (c) Brillioun zone
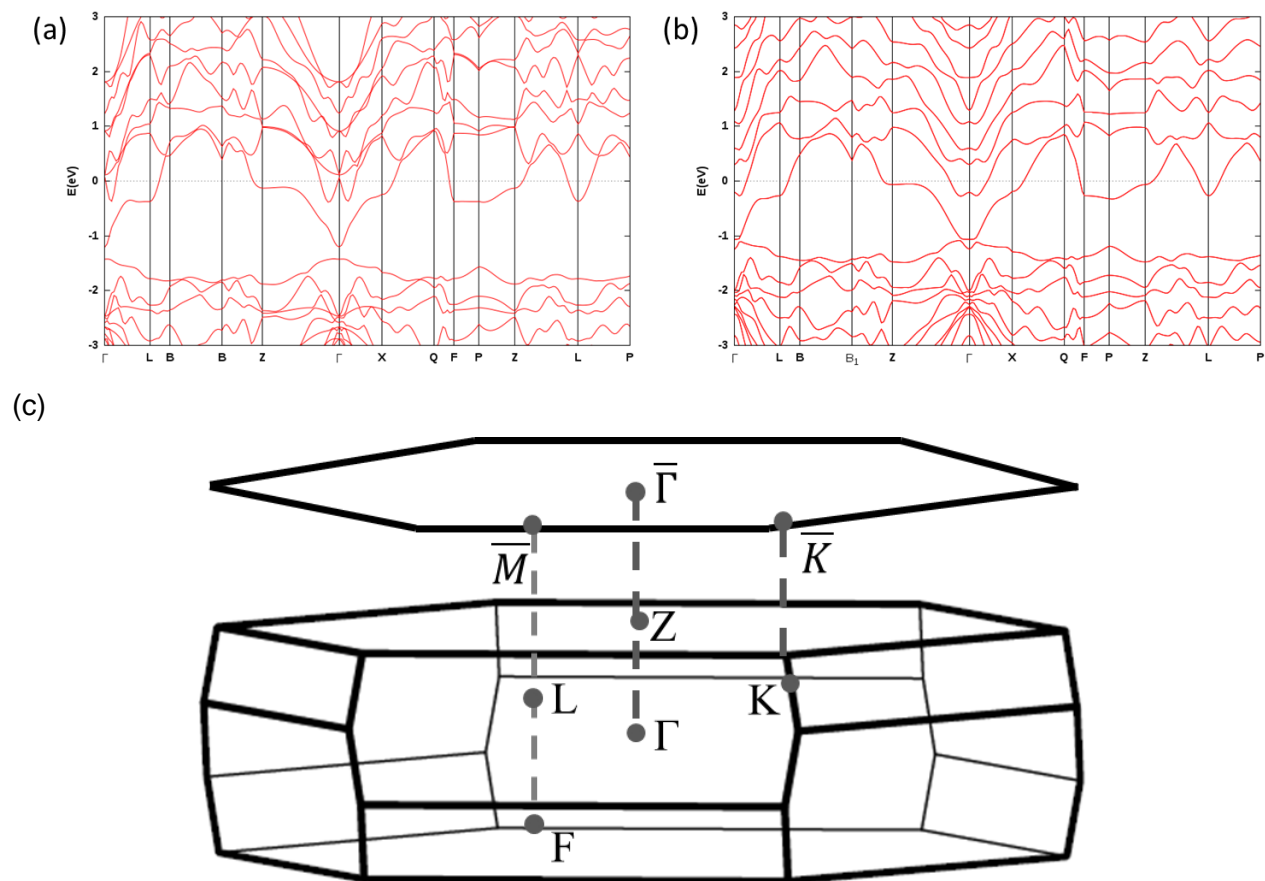
Section SII – Weyl point surface Fermi Arc calculations

Fig. S2:(a) The Weyl nodes of the bulk BZ on the (0001) surface of Bi_2MnSe_4. (b) and (c) are the calculated Fermi surface containing a pair of crescent Fermi arcs around the Γ points.
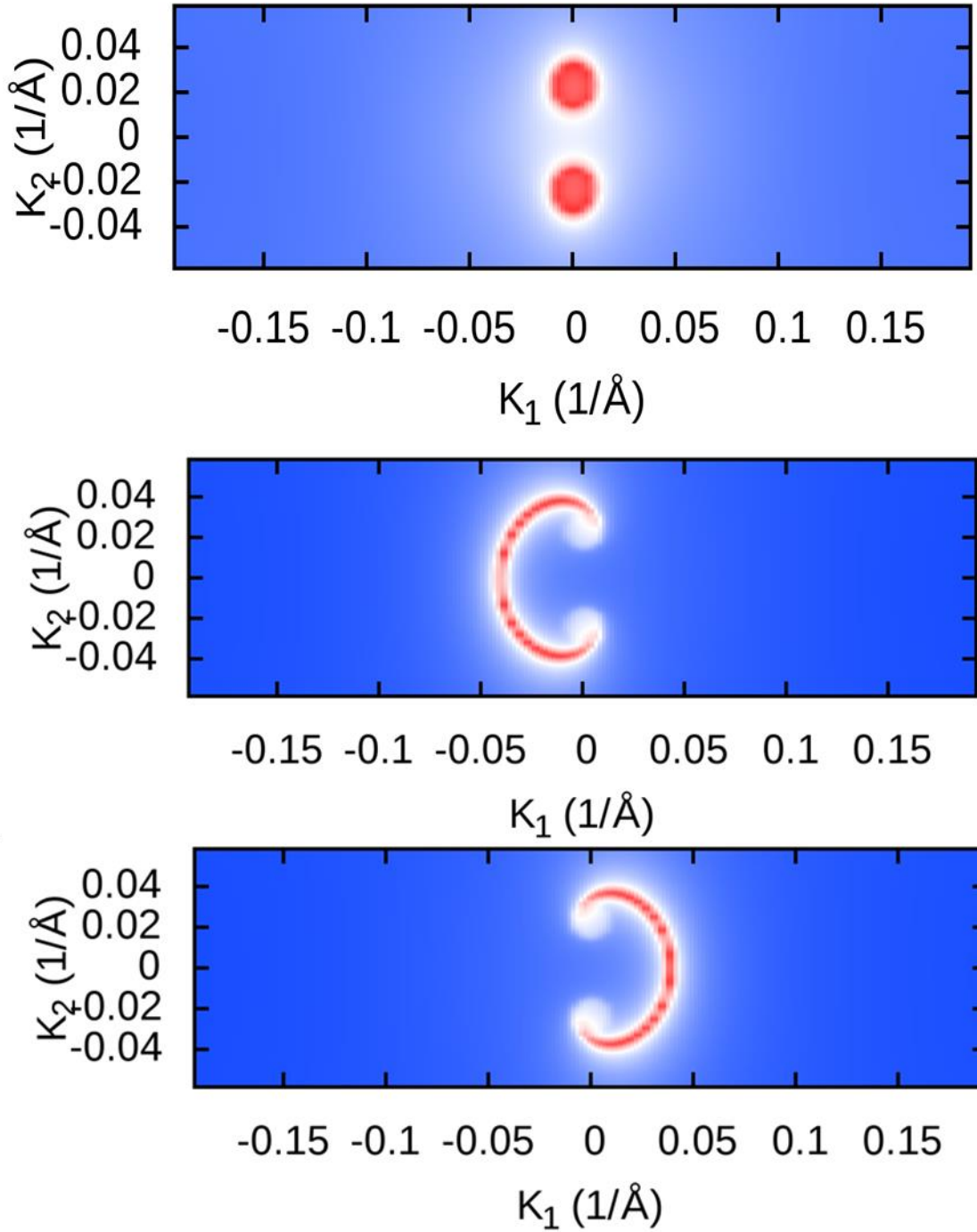
Section SIII – Supplementary Slab Figures

Fig. S3: Bandstructure of Bi atoms on ferromagnetic Bi_2MnSe_4 using different thickness with spin aligned along $\hat{z}$ direction. Red colors represent projection onto Bi-centered Wannier functions, as in main text.
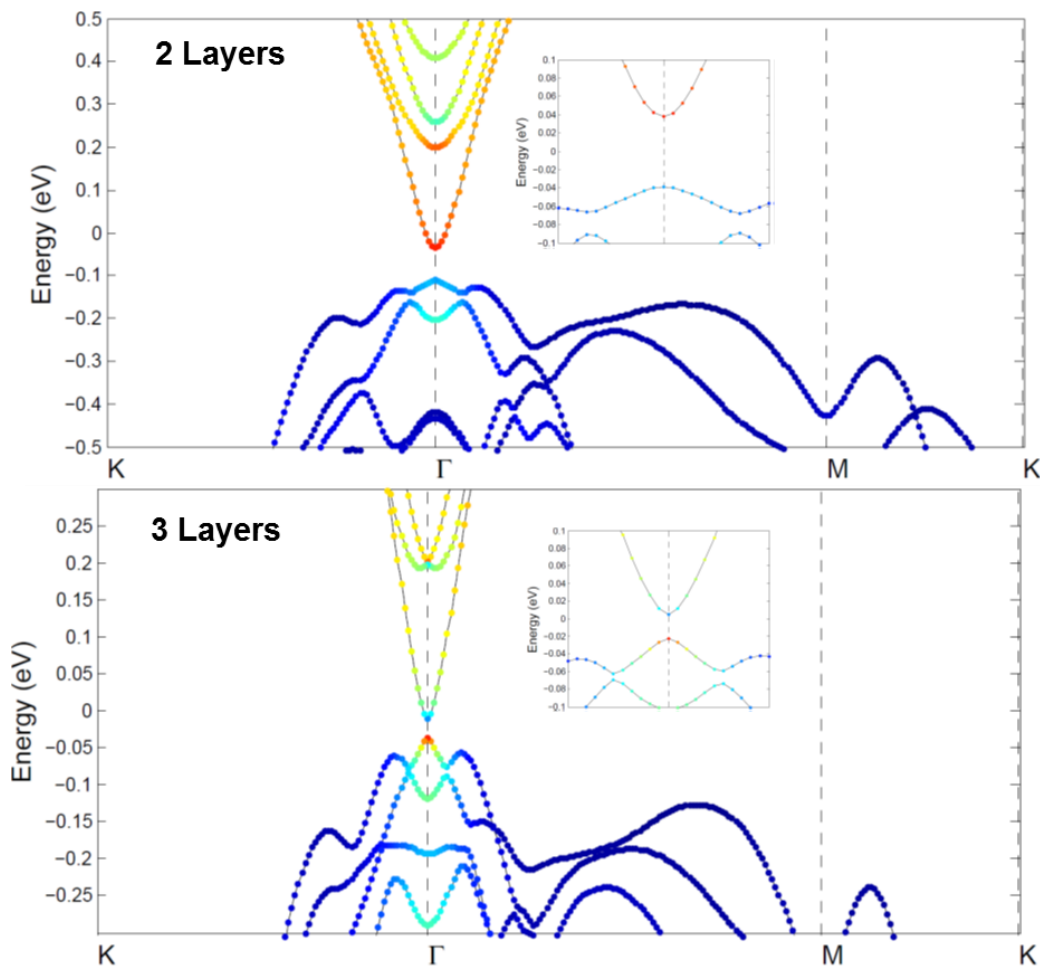
Fig. S4: Bandstructure of Bi atoms on antiferromagnetic Bi_2MnSe_4 using different thickness with spin aligned along $\hat{z}$ direction. Red colors represent projection onto Bi-centered Wannier functions, as in main text.
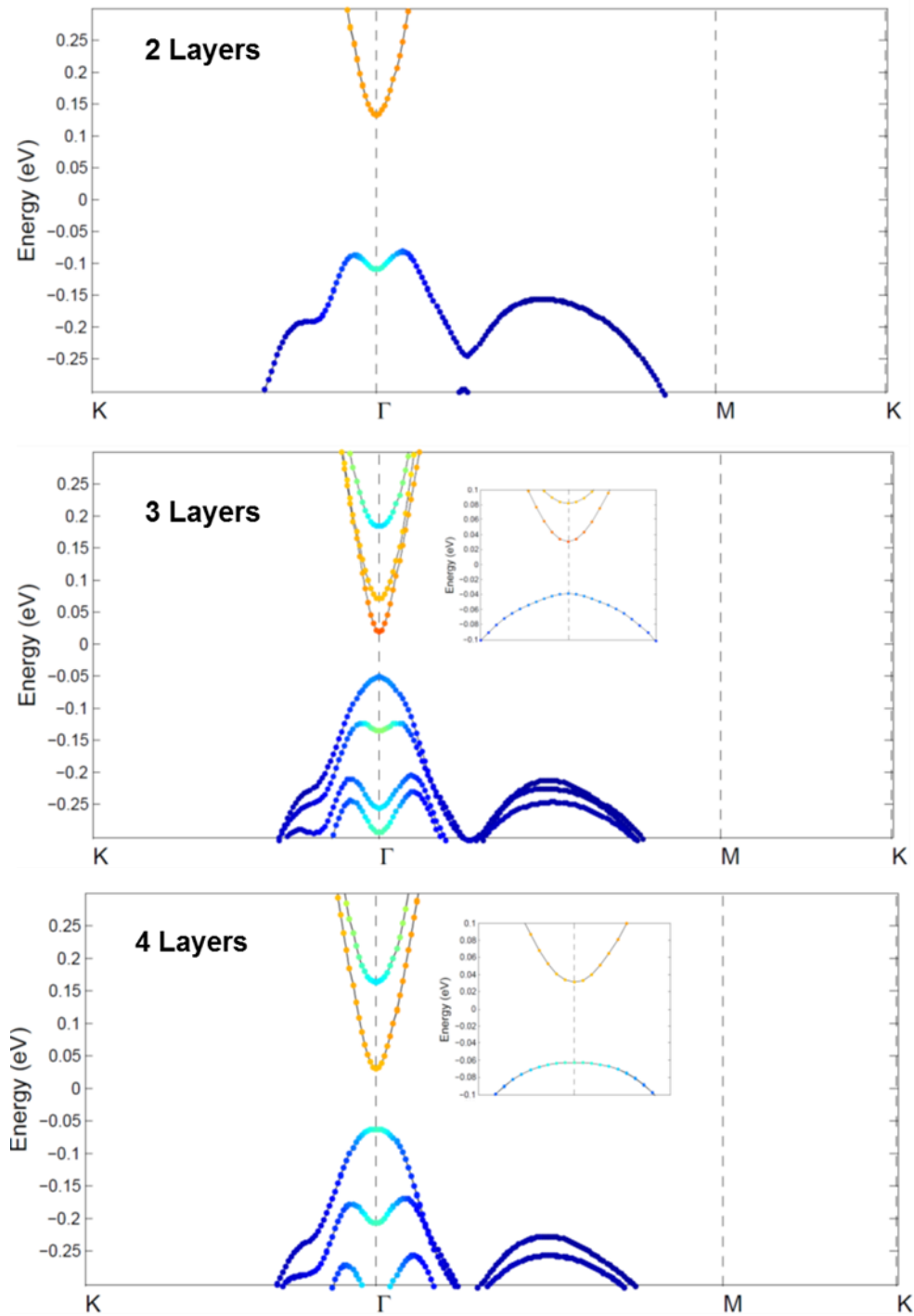
Section SIV – Simple Weyl semimetal model and discussion of Weyl physics.

Following the work of Yang et. al.[1], we introduce a simple two-band tight-binding model that clarifies several aspects of Weyl semi-metals. Similar to the ferromagnetic phase of BMS, this model breaks time-reversal symmetry but maintains inversion:

$$H_k = [2 t_x (\cos k_x - \cos k_0) + m (2 - \cos k_y - \cos k_z)]\sigma_x +$$
$$2 t_y \sin k_y \, \sigma_y + 2 t_x \sin k_z \, \sigma_z$$

where σ is the spin degree of freedom of the electron, and σ_x, σ_y, σ_z are Pauli matrices. For the values of t_x=-0.2, t_y=0.2, t_z=0.2, m=1, $k_0 = 0.2\pi$, we plot the resulting band structure in the upper panels of figure S5 using the pyth-tb code (see physics.rutgers.edu/pythtb/). As can be seen in the upper right panel, for these parameters, the model has two Weyl points at k= (+/-k_0, 0, 0). On any closed two-dimensional plane in k-space that does not intersect the Weyl points, the model is gapped. Therefore, it is possible to calculate the Chern number of the occupied band on that plane, which can be expressed as an integral over the Berry curvature:

$$C = \frac{1}{2\pi} \sum_k F_{ij}(k)$$

where F_{ij} is the Berry curvature of the occupied band and where the sum is over 2d planes of k-space. We do this for (k_y,k_z)-planes at fixed values of k_x in the lower left panel of figure S5. As can be seen, the Chern number is equal to -1 for k_x between the Weyl points, and zero otherwise. This is because the Weyl points with +/- chirality serve as sources/sinks of Berry curvature in k-space, and there is a net Berry flux in planes between the Weyl points. The AHC is expressed as an integral of the Berry curvature of the filled band over all k-space:

$$\sigma_{ij} = \left(\frac{e^2}{h}\right)\left(\frac{1}{\Omega}\right) \sum_k F_{ij}(k)$$

where Ω is the unit cell volume and the sum is over 3d k-space. Thus, for systems with a gap except at isolated points, the AHC is proportional to percentage the BZ with non-zero Chern number, which is proportional to the separation between the Weyl points in k-space. The non-zero values of the Chern number in planes of k-space also suggest a strong connection

between Weyl semimetals in 3D and Chern insulators in 2d, and this is the reason that thin films of Weyl semi-metals with surfaces perpendicular to the line between the Weyl points are promising systems to look for Chern insulators.

In the lower right panel, we calculate the surface band structure of the (010) surface of the model, in a 30 layer slab geometry. The flat bands near Γ that connect the projected Weyl points are the surface Fermi arcs, which carry the anomalous Hall conductivity. We note that if we look instead at the (100) surface, the Weyl points will be projected onto the same point of the surface band structure.

Weyl points are also possible in systems that instead have unbroken time-reversal symmetry, but broken inversion. The Weyl points in those systems are locally the same as in the broken time-reversal case. However, unbroken time-reversal symmetry requires that these systems have additional pairs of Weyl points beyond the minimum single pair in the magnetic case. These additional Weyl pairs must contribute additional AHC that results in a system with zero net AHC, as expected for systems with time-reversal symmetry. See for instance see reviews by Armitage[2] and Burkov[3].

Figure S5: Upper left: band structure of Weyl two-band model. Upper right: band structure near k = (0,0,0). Lower left: Chern number over (k_y, k_z) plane for fixed k_x. Lower left: surface band structure of (010) plane. The flat bands near Γ are Fermi arcs.
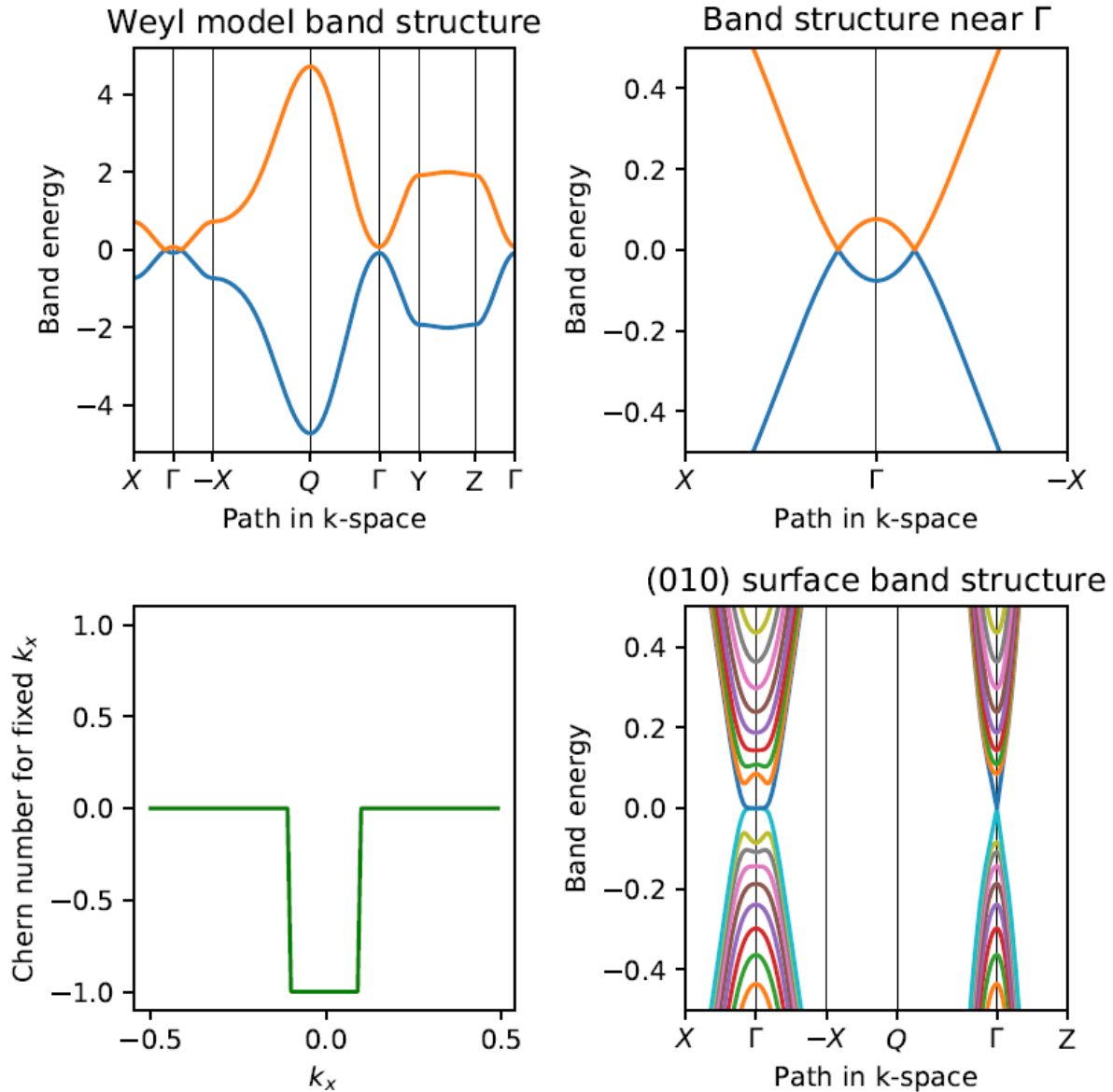
Section SV – Magnetic Ising Model and magnetic transition temperature.

In order to calculate the magnetic ordering temperature under a simple approximation, we fit the energy of various spin configurations to an Ising model, as implemented by Garrity[4].

$$H = 1\frac{1}{2}\sum_{ij} J_{ij} s_i s_j$$

where i and j run over Mn sites, $s_i = (1,-1)$ represents the direction of the spin at site i, and J_{ij} are the fitting constants. This model is appropriate for materials with large magnetic anisotropy, where the spin is forced to point along a single direction, in this case the z-direction. This approximation will tend to overestimate the transition temperature, as the spins will have some fluctuation in the x and y directions.

We fit two models, one with only nearest neighbor interactions in-plane and out-of-plane, and one with longer range interactions. We perform a least-squares fit of the parameters to calculations in 3 x 3 x 3 supercells using various spin configurations. We use recursive feature elimination and cross-validation to identify important interaction parameters when fitting the longer range model. We show the performance of the models in reproducing the DFT energies in left panel of figure S6.

Figure S6: Left: Comparison between DFT energies and Ising model energies for various magnetic orderings, relative to the FM phase. Upper right: AFM order parameter as a function of temperature. Lower right: AFM susceptibility as a function of temperature.
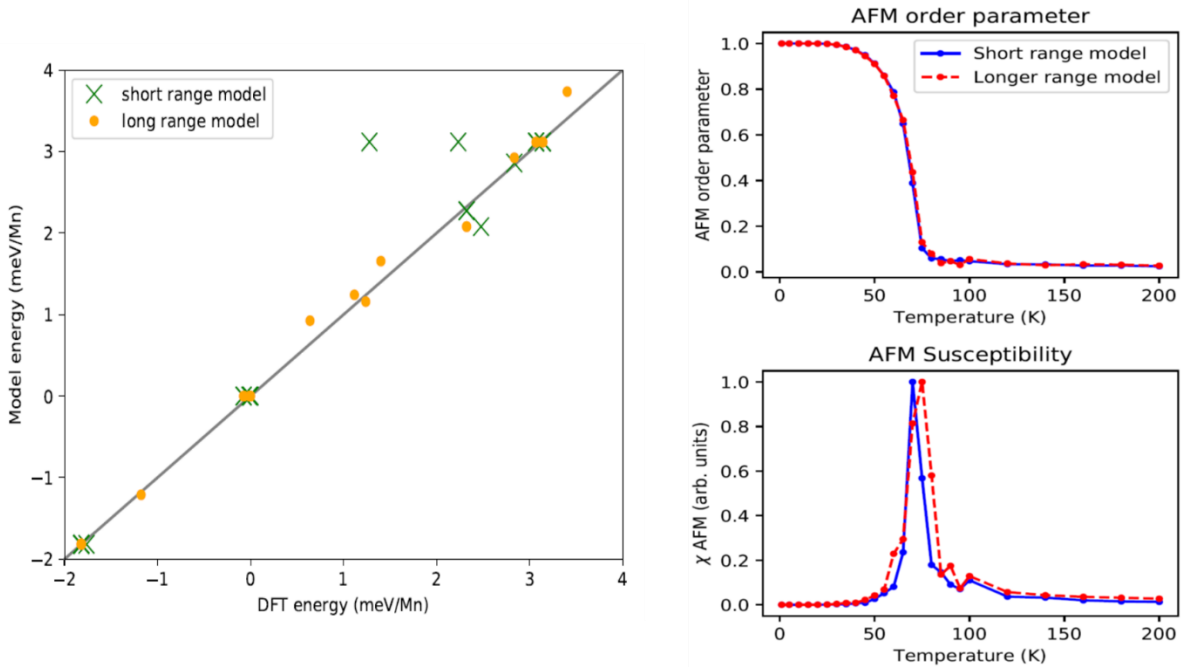
We solve the models on a 12 x 12 x 12 grid using classical Monte Carlo sampling of the Boltzmann partition function, using the Metropolis single spin flip algorithm. The results for the antiferromagnetic order parameter and susceptibility are presented in the right panels of figure S6. The transition temperature for both models is at 75 K. While we expect this to be an overestimate of the real transition temperature due to quantum effects, the large spins of Mn (5 μ_B) are often accurately treated as classical. While exactly predicting the magnetic transition temperature of a complicated material from first principles is difficult, we expect that the magnetic ordering temperature of single crystal Bi_2MnSe_4 to be several orders of magnitude above the milli-Kelvin temperature range of typical QAH materials based on Bi_2Te_3 doped with disordered magnetic atoms.

Section SVI – Layer-by-layer AHC

In fig S7, we present more details on the layer-resolved contributions to the AHC in the AFM phase using a thick slab geometry, using the method describe by Rauch[5]. We solve the tight-binding model on a 128 x 128 k-point grid. We present results for a 31 layer slab with C=1 number (solid blue line) and a 32 layer slab with C=0. In the upper left panel, we show the simple layer-by-layer contributions. There is both an overall trend and sharp oscillations between spin up and spin down layers. In the upper right panel, we average over pairs of layers, which eliminates the oscillatory behavior and shows the contributions to the AHC decaying as towards the center of the slab.

In the lower left and lower right panels, we present the cumulative contribution the AHC, summing over layers, with the right panel again averaging pairs of layers. We can see that in both the C = 1 and C = 0 cases, the bottom surface contributes a total of +0.5($\frac{e^2}{h}$) to the AHC. In the odd layer C=1 case, the top surface also contributes +0.5 for a net +1.0 ($\frac{e^2}{h}$), but in the even layer C=0 case, the top surface contributes -0.5, for a total slab AHC of 0.0 ($\frac{e^2}{h}$), as expected for a C=0 material.

Figure S7: Upper left: Surface AHC, separated into layers, for 31 layer slab (solid blue) and 32 layer slab (dashed red). Upper right: Surface AHC separated into layers and averaged over pairs of layers. Lower left: Cumulative AHC summing over layers. Lower right: Cumulative AHC averaged over pairs of layers.
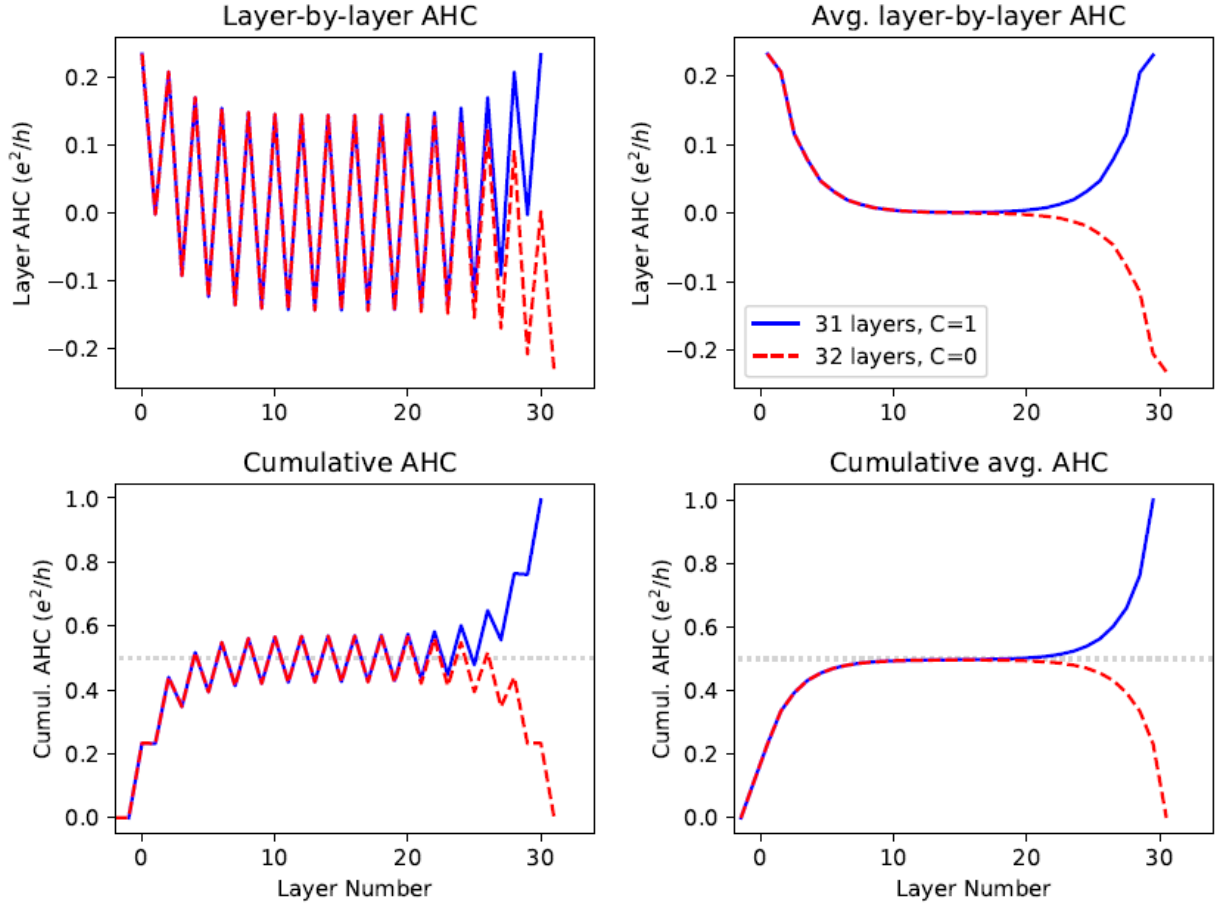
Section SVII – Wannier charge centers for AFM phase

We calculate the topological invariant of the bulk AFM phase by computing Wannier charge center (WCC) positions. We show that the $k_3=0$ Wannier charge centers switch partners going from $k_2 = 0$ to $k_2 = 0.5$, characteristic of a non-trivial topological phase and a theta value of π, as discussed by Taherinejad[6], Soluyanov[7] and Mong[8].

Figure S8: Evolution of Wannier charge centers along direction 1 while varying parameter k_2, with k_3 fixed to 0.0 (left) and 0.5 (right). The left panel shows non-trivial partner switching.
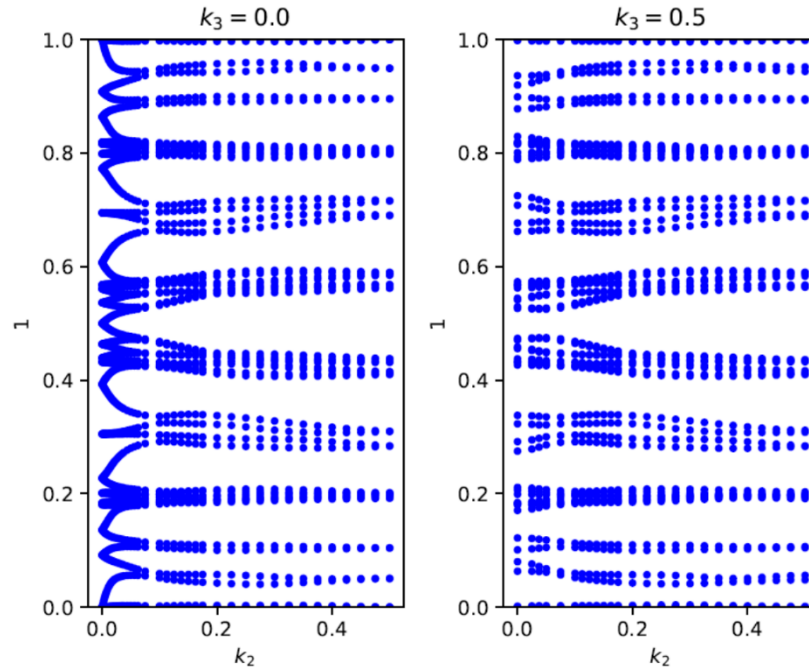


Section SVIII – Hybrid functional calculations

In order to better understand how robust our results are to alternate approximations, we perform hybrid functional HSEsol[9] calculations, as implemented in VASP[10,11], studying the effect of different fractions of exact exchange (EXX) on our results. While hybrid functionals produce on average better semiconductor band gaps than semi-local functionals, which tend to underestimate band gaps, the necessary fraction of exact exchange can vary across materials classes. Metals and small gap materials sometimes give worse results for x=0.25, the default value of EXX in HSE.

In particular, the effects of hybrid functionals have been explored in Bi_2Se_3 and related compounds previously[12]. That work finds that hybrid functionals on average tend to worsen agreement with the experimental band structures of these topological insulators. We reproduce this finding in the left panel figure S9, which shows that x=0.25 over-corrects the band gap of Bi_2Se_3, reducing the amount of band inversion and therefore reducing the inverted band gap at k=Γ. Better agreement with experiment[13] is achieved for x~0.07. These results are consistent with the large electronic dielectric constant of Bi_2Se_3, 28.0 in our non-SOC linear response

calculations, which translates to a EXX fraction of 0.035 using the non-self-consistent method of Skone et. al[14].

In the right panel of figure S9, we consider the effects of EXX on the bands at k=Γ in the ferromagnetic Weyl semimetal phase of Bi_2MnSe_4. As expected, increasing EXX reduces the overlap between Bi and Se states. The $Γ_{5+}$ and $Γ_{4+}$ bands, which have Bi character, rise above the Se-like $Γ_{5-}$ and $Γ_{4-}$ bands with increasing EXX. For EXX fraction above 0.115, the bands cross and the material becomes a trivial insulator. Using the value of EXX preferred by our Bi_2Se_3 results, Bi2MnSe4 remains in the Weyl semimetal phase using hybrid functional calculations.

Figure S9: Left panel: Direct band gap at Γ of Bi_2Se_3 as a function of EXX for HSEsol unctional. Right panel: Changes of 4 bands at Γ in FM phase of BMS as a function of EXX. BMS is a Weyl semimetal for EXX < 0.115 and trivial for larger EXX.
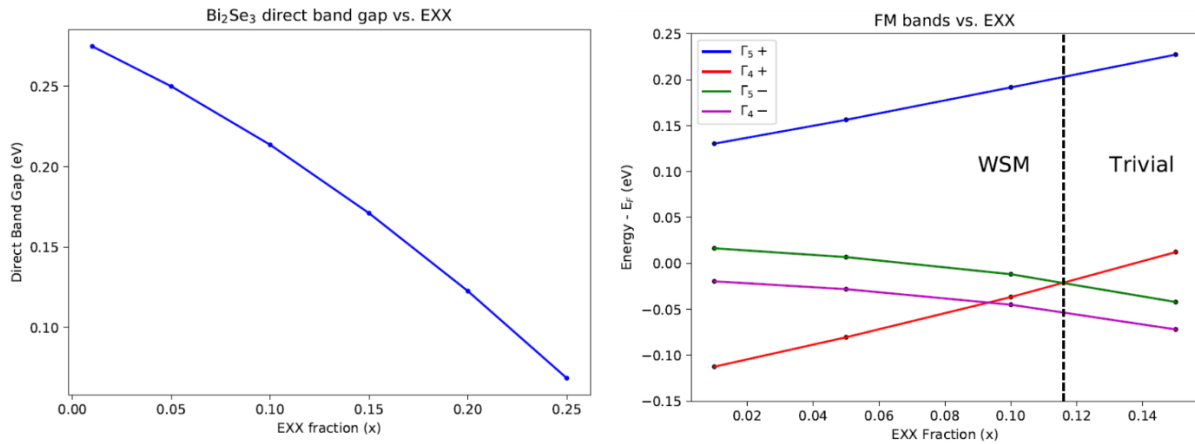
Section SIX – (100) AFM Surface state

Unlike the (001) surface, which breaks time reversal symmetry, other surfaces of the BMS AFM TI phase can show non-trivial surface states[8]. In figure S10, we present the tight-binding based surface bands on the (100) surface, which shows a nontrivial feature.

Figure S10: Energy and momentum dependence of local density of states (LDOS) of the (100) surface of the AFM phase of BMS. Here, the red region shows the bulk energy bands and the blue region shows the energy gap.
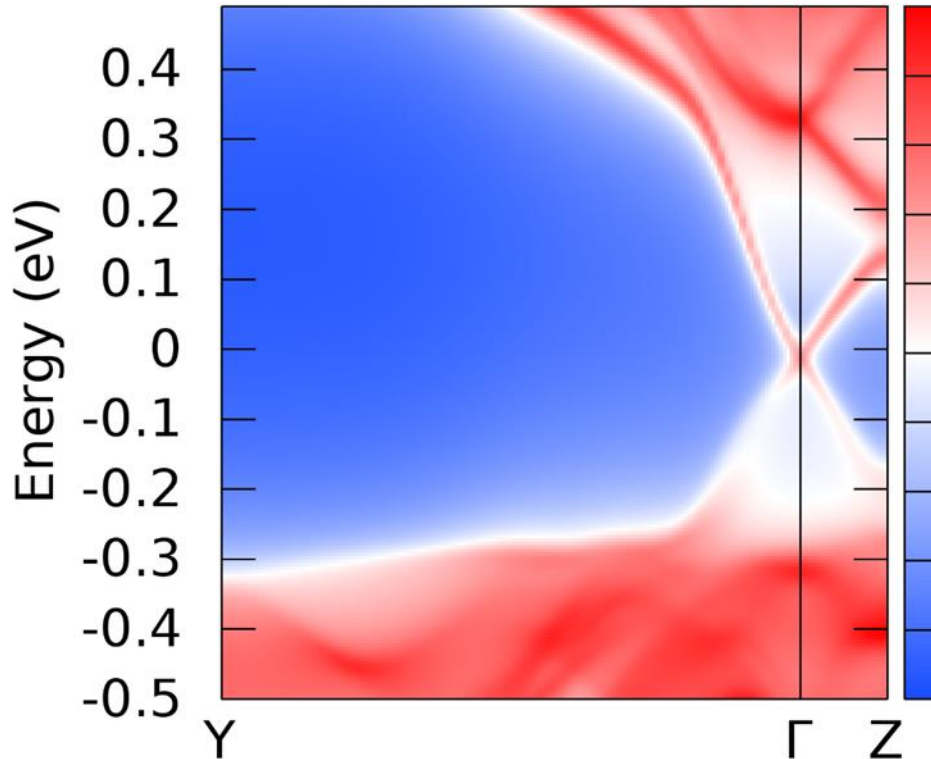
Reference:

1   Yang, K.-Y., Lu, Y.-M. & Ran, Y. Quantum Hall effects in a Weyl semimetal: Possible application in pyrochlore iridates. *Physical Review B* **84**, 075129 (2011).

2   Armitage, N., Mele, E. & Vishwanath, A. Weyl and Dirac semimetals in three-dimensional solids. *Reviews of Modern Physics* **90**, 015001 (2018).

3   Burkov, A. & Balents, L. Weyl semimetal in a topological insulator multilayer. *Physical review letters* **107**, 127205 (2011).

4   Garrity, K. F. Combined cluster and atomic displacement expansion for solid solutions and magnetism. *arXiv preprint arXiv:1808.00090* (2018).

5   Rauch, T., Olsen, T., Vanderbilt, D. & Souza, I. Geometric and nongeometric contributions to the surface anomalous Hall conductivity. *arXiv preprint arXiv:1806.01707* (2018).

6   Taherinejad, M., Garrity, K. F. & Vanderbilt, D. Wannier center sheets in topological insulators. *Physical Review B* **89**, 115102 (2014).

7   Soluyanov, A. A. & Vanderbilt, D. Computing topological invariants without inversion symmetry. *Physical Review B* **83**, 235401 (2011).

8   Mong, R. S., Essin, A. M. & Moore, J. E. Antiferromagnetic topological insulators. *Physical Review B* **81**, 245209 (2010).

9   Heyd, J., Scuseria, G. E. & Ernzerhof, M. Hybrid functionals based on a screened Coulomb potential. *The Journal of chemical physics* **118**, 8207-8215 (2003).

10   Kresse, G. & Hafner, J. Ab initio molecular dynamics for liquid metals. *Physical Review B* **47**, 558 (1993).

11   Kresse, G. & Joubert, D. From ultrasoft pseudopotentials to the projector augmented-wave method. *Physical Review B* **59**, 1758 (1999).

12   Park, S. & Ryu, B. Hybrid-density functional theory study on the band structures of tetradymite-Bi 2 Te 3, Sb 2 Te 3, Bi 2 Se 3, and Sb 2 Se 3 thermoelectric materials. *Journal of the Korean Physical Society* **69**, 1683-1687 (2016).

13   Martinez, G. *et al.* Determination of the energy band gap of Bi 2 Se 3. *Scientific reports* **7**, 6891 (2017).

14   Skone, J. H., Govoni, M. & Galli, G. Self-consistent hybrid functional for condensed systems. *Physical Review B* **89**, 195112 (2014).

1   Yang, K.-Y., Lu, Y.-M. & Ran, Y. Quantum Hall effects in a Weyl semimetal: Possible application in pyrochlore iridates. *Physical Review B* **84**, 075129 (2011).

2   Armitage, N., Mele, E. & Vishwanath, A. Weyl and Dirac semimetals in three-dimensional solids. *Reviews of Modern Physics* **90**, 015001 (2018).

3   Burkov, A. & Balents, L. Weyl semimetal in a topological insulator multilayer. *Physical review letters* **107**, 127205 (2011).

4   Garrity, K. F. Combined cluster and atomic displacement expansion for solid solutions and magnetism. *arXiv preprint arXiv:1808.00090* (2018).

5   Rauch, T., Olsen, T., Vanderbilt, D. & Souza, I. Geometric and nongeometric contributions to the surface anomalous Hall conductivity. *arXiv preprint arXiv:1806.01707* (2018).

6   Taherinejad, M., Garrity, K. F. & Vanderbilt, D. Wannier center sheets in topological insulators. *Physical Review B* **89**, 115102 (2014).

7   Soluyanov, A. A. & Vanderbilt, D. Computing topological invariants without inversion symmetry. *Physical Review B* **83**, 235401 (2011).

8   Mong, R. S., Essin, A. M. & Moore, J. E. Antiferromagnetic topological insulators. *Physical Review B* **81**, 245209 (2010).

9   Heyd, J., Scuseria, G. E. & Ernzerhof, M. Hybrid functionals based on a screened Coulomb potential. *The Journal of chemical physics* **118**, 8207-8215 (2003).

10   Kresse, G. & Hafner, J. Ab initio molecular dynamics for liquid metals. *Physical Review B* **47**, 558 (1993).

11   Kresse, G. & Joubert, D. From ultrasoft pseudopotentials to the projector augmented-wave method. *Physical Review B* **59**, 1758 (1999).

12   Park, S. & Ryu, B. Hybrid-density functional theory study on the band structures of tetradymite-Bi 2 Te 3, Sb 2 Te 3, Bi 2 Se 3, and Sb 2 Se 3 thermoelectric materials. *Journal of the Korean Physical Society* **69**, 1683-1687 (2016).

13   Martinez, G. *et al.* Determination of the energy band gap of Bi 2 Se 3. *Scientific reports* **7**, 6891 (2017).

14   Skone, J. H., Govoni, M. & Galli, G. Self-consistent hybrid functional for condensed systems. *Physical Review B* **89**, 195112 (2014).